Electronic Supplementary Information (ESI)

Triflate anion chemistry for enhanced four-electron zinc–iodine aqueous batteries

Tingting Liu, Chengjun Lei, Huijian Wang, Wei Yang, Xin He, Xiao Liang*

State Key Laboratory of Chem/Bio-Sensing and Chemometrics, Advanced Catalytic Engineering Research Center of the Ministry of Education, College of Chemistry and Chemical Engineering, Hunan University, Changsha, Hunan, 410082, China

E-mail: xliang@hnu.edu.cn

Experimental section

All reagents and starting materials were used as received without any further purification. iodine powder (I_2), Zinc iodide (ZnI_2), Lithium Trifluoromethanesulfonate (LiOTf), acetonitrile (ACN), iodine monochloride (ICl) and porous activated carbon were purchased from Aladdin. Zinc chloride ($ZnCl_2$) was purchased from Sigma-Aldrich.

Synthesis of AC/I_2 composites

The iodine composites were prepared using "solution- adsorption" method. The obtained AC was mixed with iodine at a weight ratio of 1:3, followed by putting into 20 ml deionized water with ultrasonic dispersion for 2 hours. The suspension was aged at 60 ℃ for 12 hours for the iodine adsorption before the filtration. The composites were dried at 45 ℃.

Characterization of Physicochemical Properties

Powder X-ray diffraction (XRD) was performed on D8 ADVANCE with Cu Kα radiation at a scan rate of 10 ℃ min^{-1} in 40KV, 30mA. Scanning electron microscope (SEM) was carried out on MIRA4 LMH. Raman analysis was taken with a bench Raman dispersive microspectrometer (InVia Reflex, Renishaw) using a laser (wavelength of 532 nm). UV-vis data was collected on UV1902PC with the range from 190-600nm. Thermo gravimetric analysis (TGA) was analysed on HTG-1 under Argon with 10 ℃ min^{-1}. X-ray hotoelectron spectroscopy (XPS) analysis was recorded on AXIS SUPRA using an Al Kα source.

Electrochemical measurements

The working electrodes were made by mixing the obtained AC/I_2, acarboxymethylcellulose (CMC) binder and super P agents with a mass ratio of 7:2:1 using deionized water, then the slurry was casted on titanium foil (current collector) and dried at 45 ℃ for 12 h in air. The cathodes were obtained with iodine loading 2-3 mg cm^{-2}. The electrolyte formula we defined is the blends of specific molality of $ZnCl_2$, LiOTF in water (donated as 2-8; 2-16 hybrid electrolytes). Swagelok-type or coins cells were assembled with zinc foil anode (0.1 mm thickness, 12 mm in diameter) glass fiber separator (Whatman GF/A, 12 mm in diameter) and AC/I_2 cathode (12 mm in diameter) with 60 μL electrolyte. The pouch cell was assembled with Zn plate anode (0.1 mm thickness, 4*3

cm), glass fiber separator (Whatman GF/A, 4.5*4.5 cm) and AC/I_2 electrodes (4*3 cm) with 2 mL electrolyte. CV tests were studied on VMP-3 workstation (Bio-logic). For Tafel tests, Zn||Zn symmetric cells with different electrolytes were controlled potential from –0.15 V to 0.15 V (vs. Open circuit voltage) at 1 mV s^{-1} scan rate.

Computational methods

All molecular dynamics (MD) simulations were performed within the Forcite Package. The COMPASS II force-field was used. The Ewald and atom-based methods were employed to analyze the Coulomb and van der Waals (VDW) interactions. Geometry optimization was realized by using the Smart method with an energy convergence criterion of 2.0×10^{-5} kcal·mol^{-1}. To further equilibrate the model, the simulations were initially relaxed at a room temperature and atmospheric pressure for 100 ps. During the simulation, Nose thermostat and Berendsen barostat algorithm were applied in the temperature and pressure control. Later, the equilibrated simulations run at constant NVT ensemble for 400 ps in order to get authentic data. All density functional theory (DFT) calculations were spin polarized and carried out with the Perdew–Burke–Ernzerhof (PBE) functional in the DMol3 Package. The Grimme correction method was employed in order to include van der Waals (vdW) interactions. The DFT semi-core pseudopot replaced the core electrons treatment. For the calculations of total energy, a global orbital cutoff of 4.4 Å, was set and the convergence tolerance of the energy, force, and displacement below 1.0×10^{-5} Ha, 2.0×10^{-3} Ha/Å, 5.0×10^{-3} Å were used for structural optimizations. For the calculation of hydrolysis energy diagrams, the salt effect is deeply considered using the slab model. The multiple complete linear synchronous transit and quadratic synchronous transit (LST/QST) method was used to find a transition state (TS) when reasonable structures for the reactants and products exist. The calculations were performed under the implicit solvent model (COSMO).
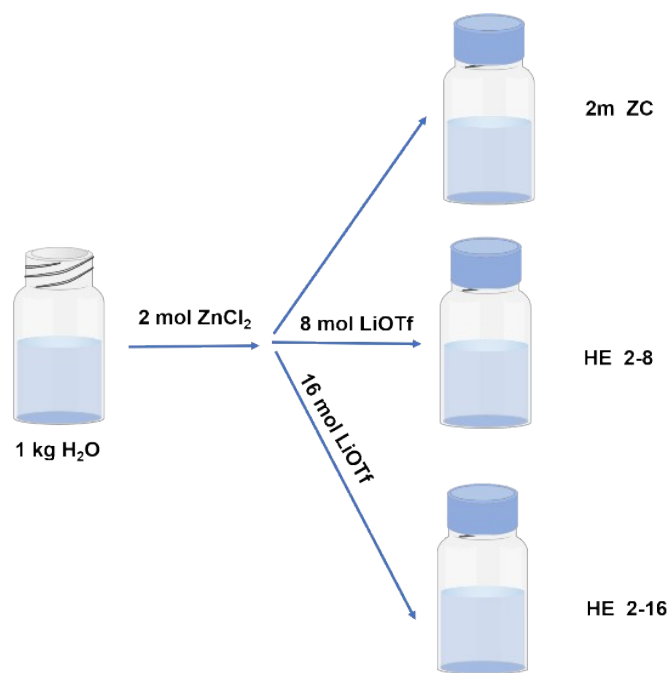
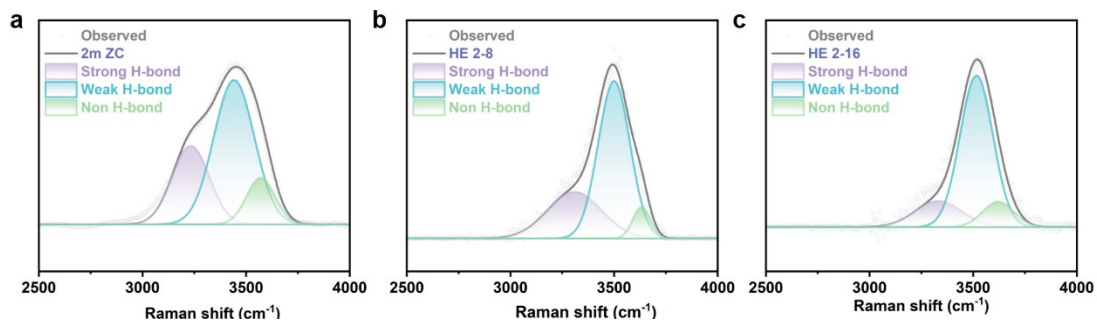**Fig. S1**. Scheme of synthesis process of different electrolytes.

Fig. S2. The fitted peaks of Raman spectroscopy representing the O-H stretching vibration of water molecules in different electrolyte, respectively.
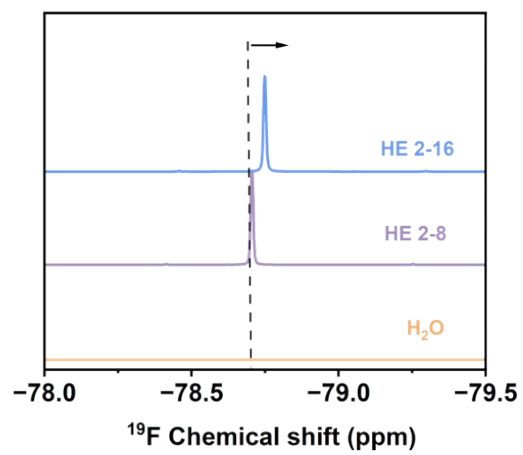
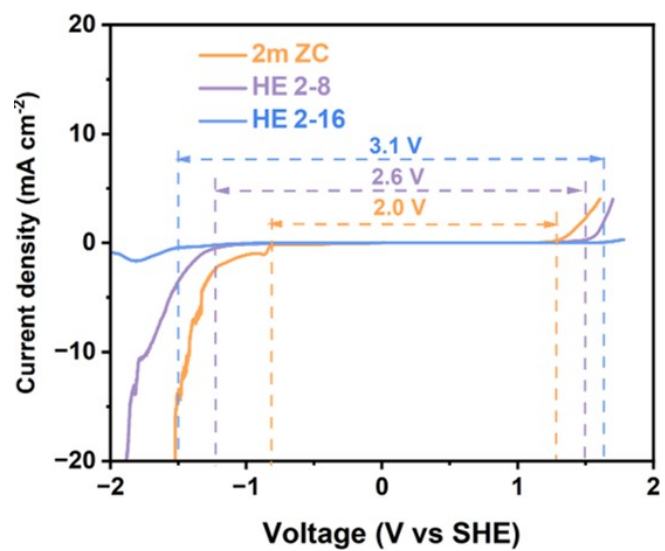**Fig. S3**. The ^{19}F NMR spectra of different electrolytes.

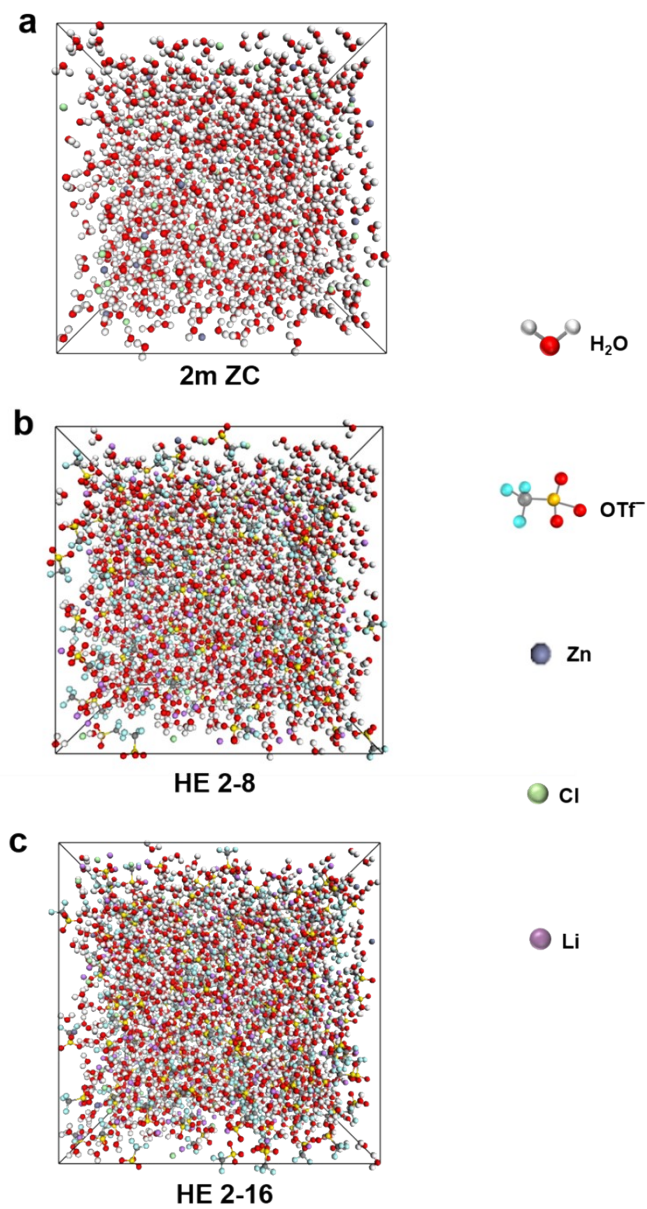**Figure S4.** The electrochemical windows of various electrolytes

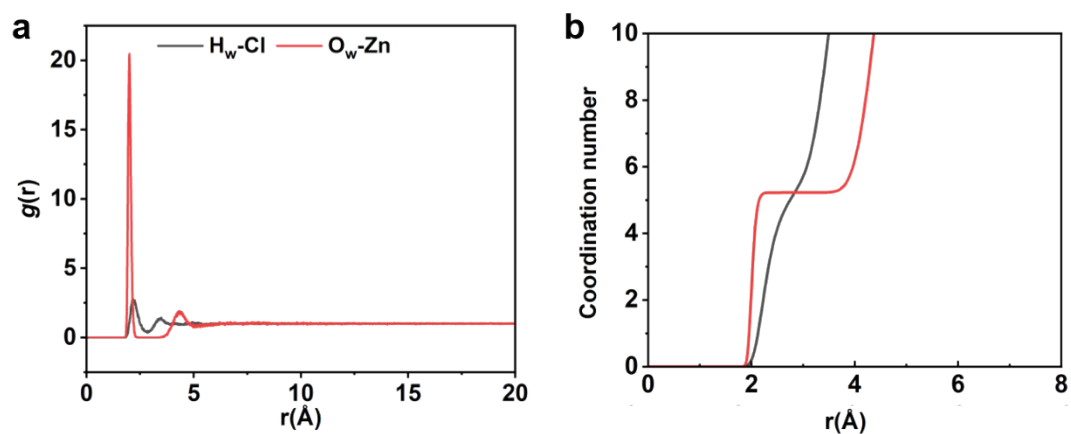**Fig. S5**. Snapshot of molecular dynamics simulations of the electrolytes structure.

Fig. S6. (a) radial distribution functions and (b) coordination number of H_2O, Cl^- and OTf^- around H_2O obtained from MD simulations for ZC.
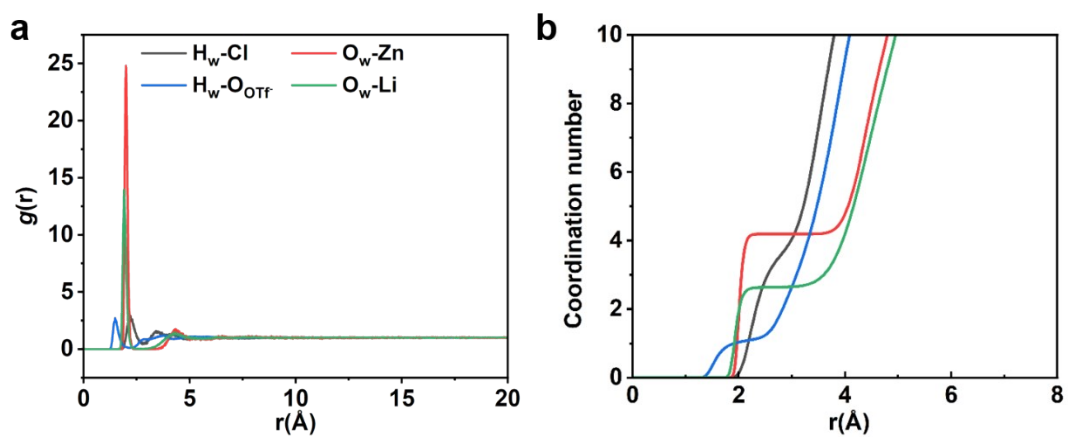
Fig. S7. (a) radial distribution functions and (b) coordination number of H_2O, Cl^-, OTf^- and Li^+ around H_2O obtained from MD simulations for HE 2-8.
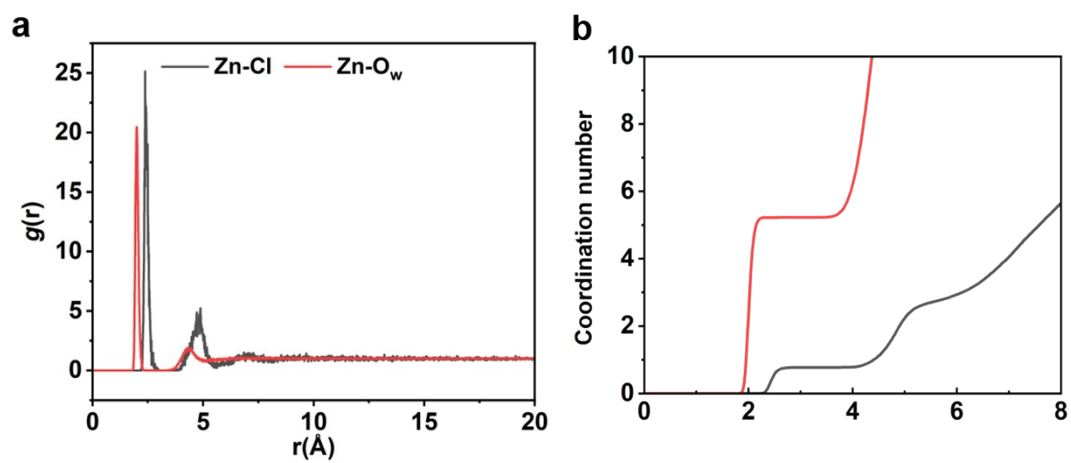
Fig. S8. (a) radial distribution functions and (b) coordination number of H_2O and Cl^- around Zn^{2+} obtained from MD simulations for ZC.
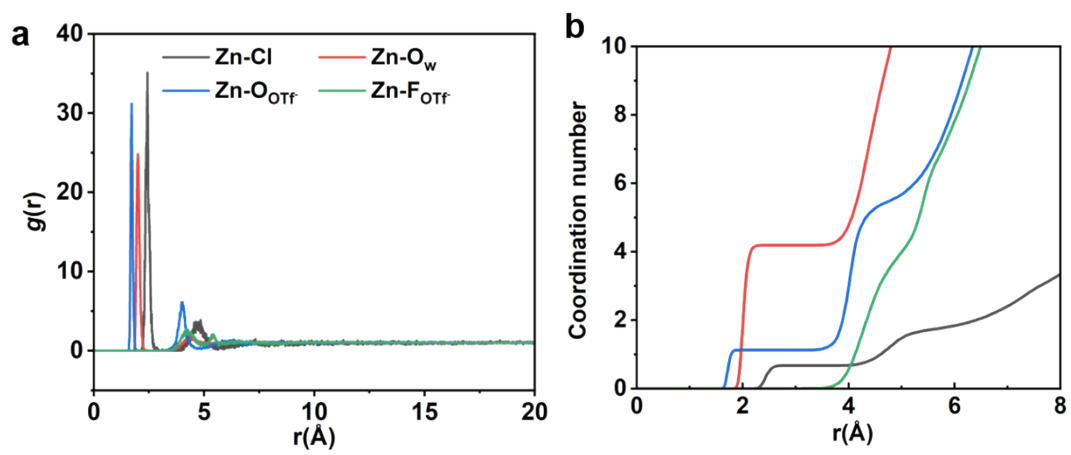
Fig. S9. (a) radial distribution functions and (b) coordination number of H_2O, Cl^- and OTf^- around Zn^{2+} obtained from MD simulations for HE 2-8.
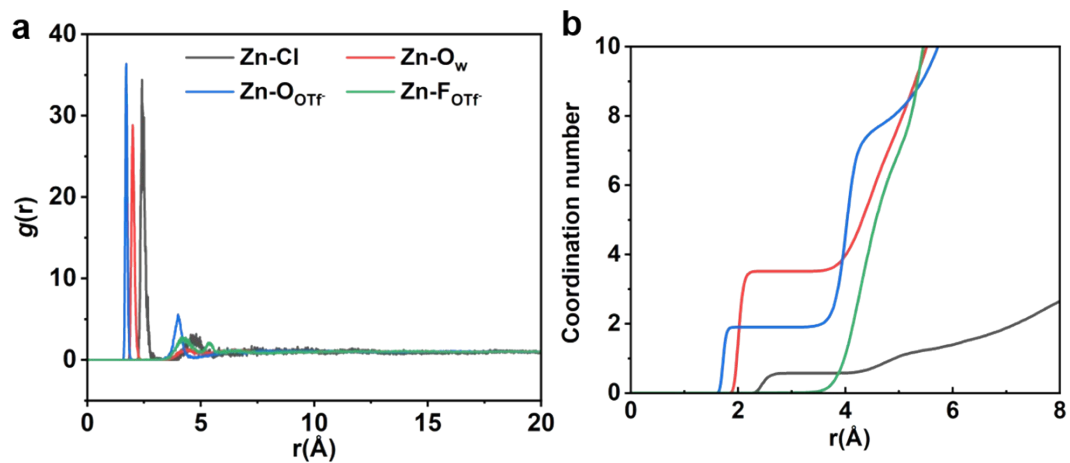
Fig. S10. (a) radial distribution functions and (b) coordination number of H_2O, Cl^- and OTf^- around Zn^{2+} obtained from MD simulations for HE 2-16.
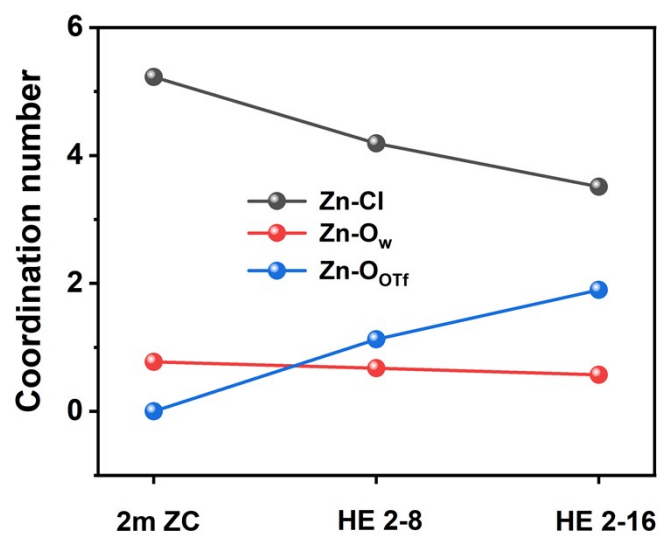
Fig. S11. Coordination numbers of H_2O, OTf^- and Cl^- around Zn^{2+}.
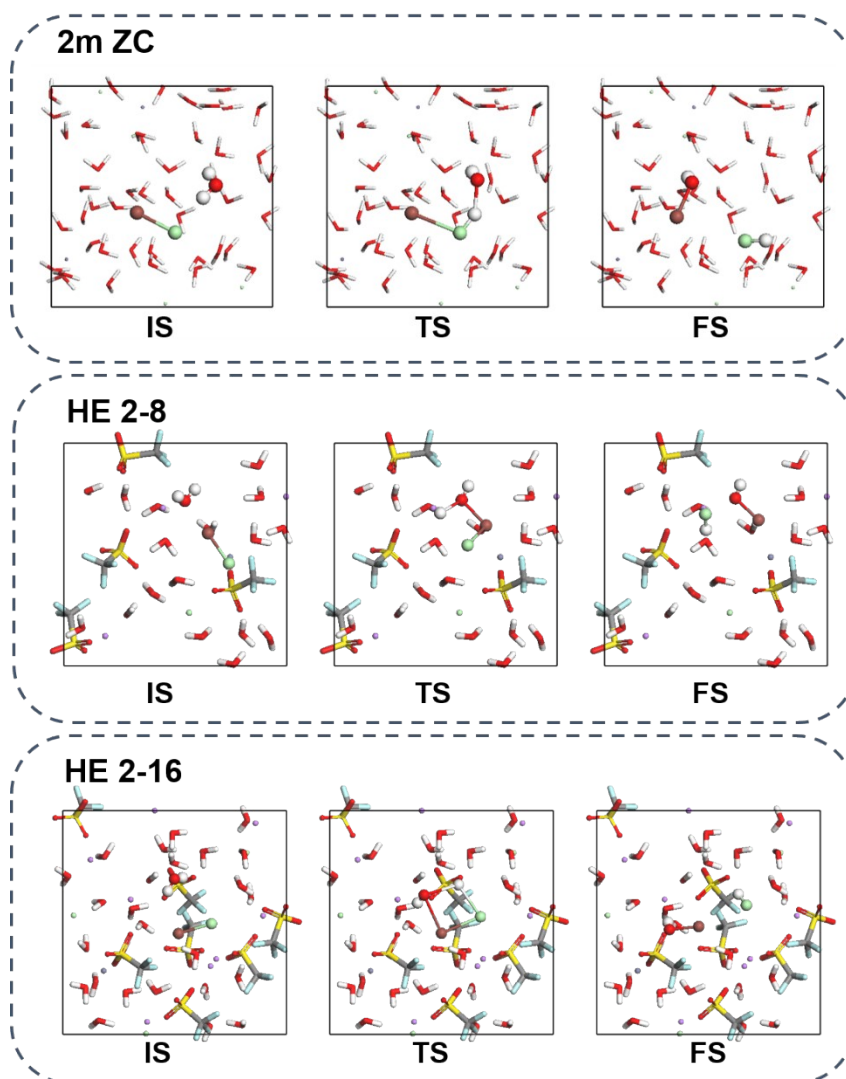
Fig. S12. The initial, transition, and final structures (IS, TS, FS) from hydrolysis reaction of ICl with different electrolyte.
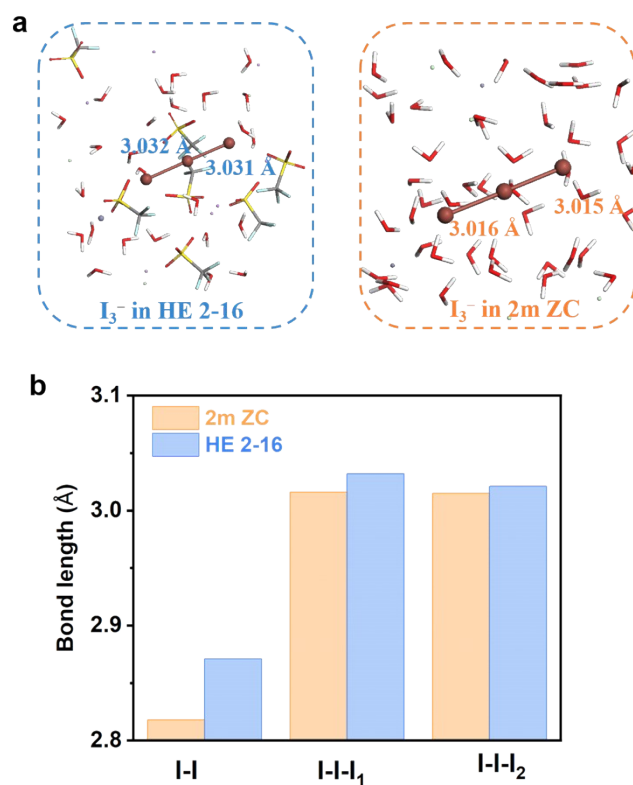
Fig. S13. (a)The optimized conformations of I_3^- species in HE 2-16 and ZC electrolyte. (b) The bond length of different species in various electrolytes.
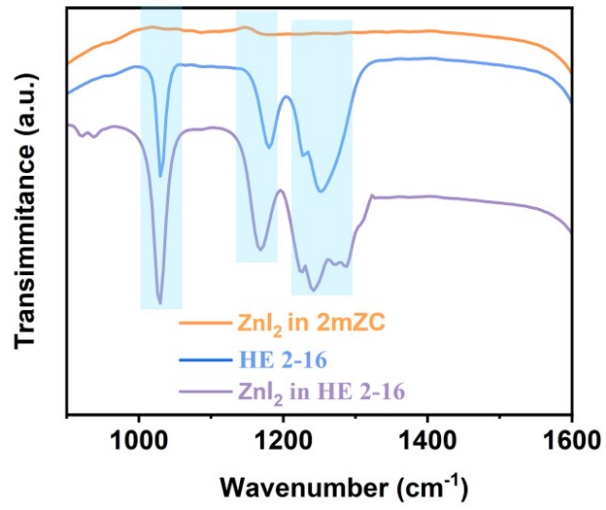
Fig. S14. FTIR spectra of HE 2-16 and ZnI_2 in ZC/HE 2-16.
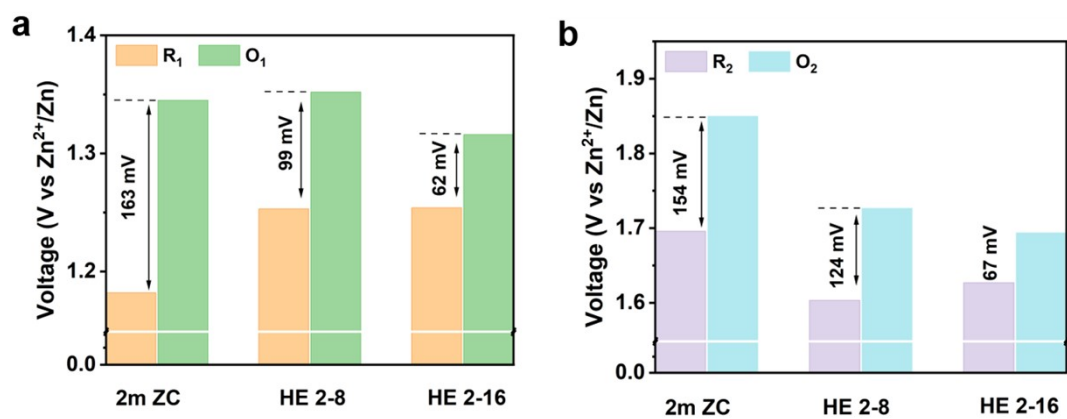
Fig. S15. The reduction and oxidation peak voltage and voltage gap determined from CV curves in **Fig. 3g**.
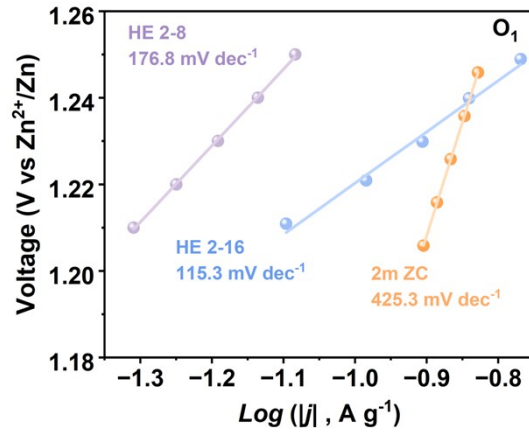
Fig. S16. The comparison of Tafel scope of different electrolytes of O_1.
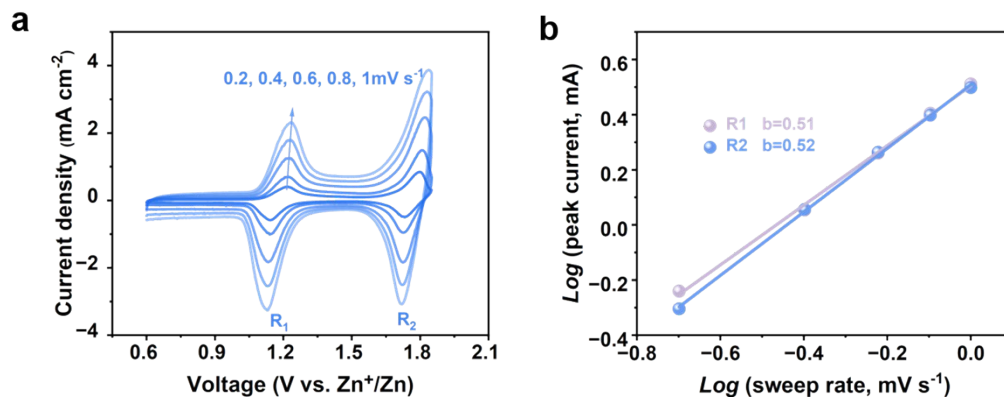
Fig. S17. (a) CV curves in HE 2-16 electrolyte at different sweep rates. (b) the plots of log i vs log ν, data was collected from CV curves.
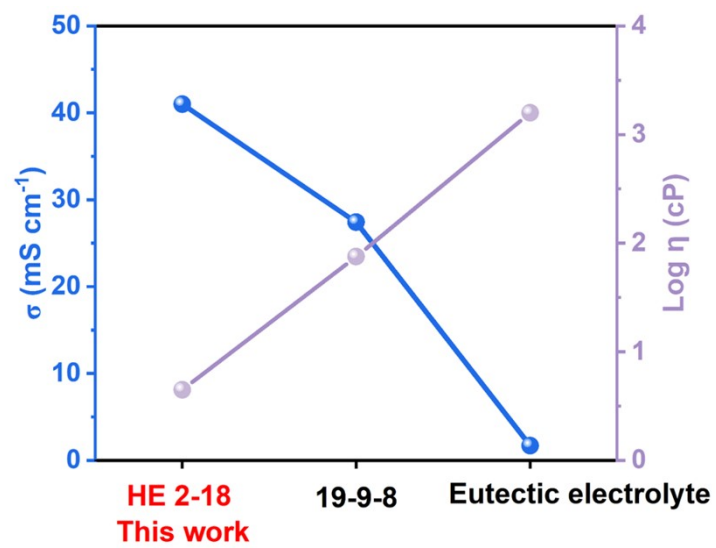
Fig. S18. The viscosity and ionic conductivity at 25 °C for the proposed HE 2-18 electrolyte and other electrolytes used in 4eZIBs.

Fig. S19. The iodine utilization ratio of 4eZIBs with different electrolytes.

Fig. S20. (a) Charge and discharge voltage profiles of the HE 2-16 electrolyte from 1.25 to 1.8 V at 400 mA g^{-1}. (b) Raman spectra of 0.05 M ICl standard solution and the E-extracted solution been charged to 1.8 V of AC/I$_2$ batteries.

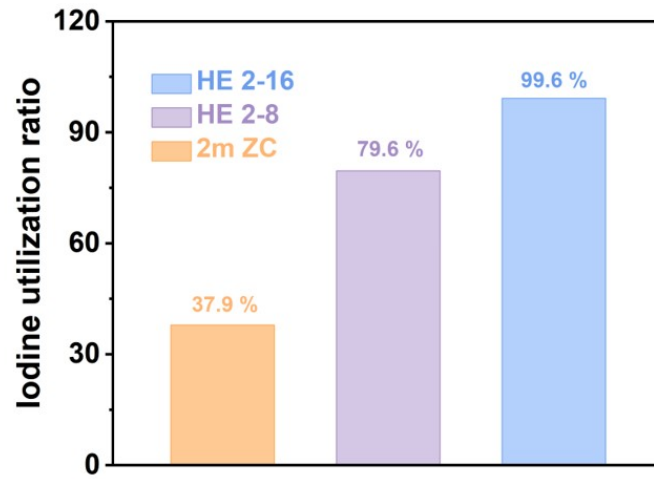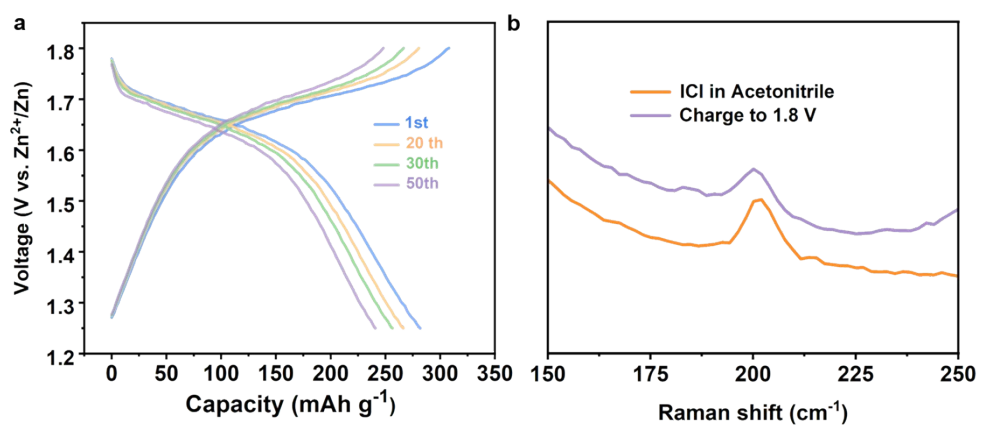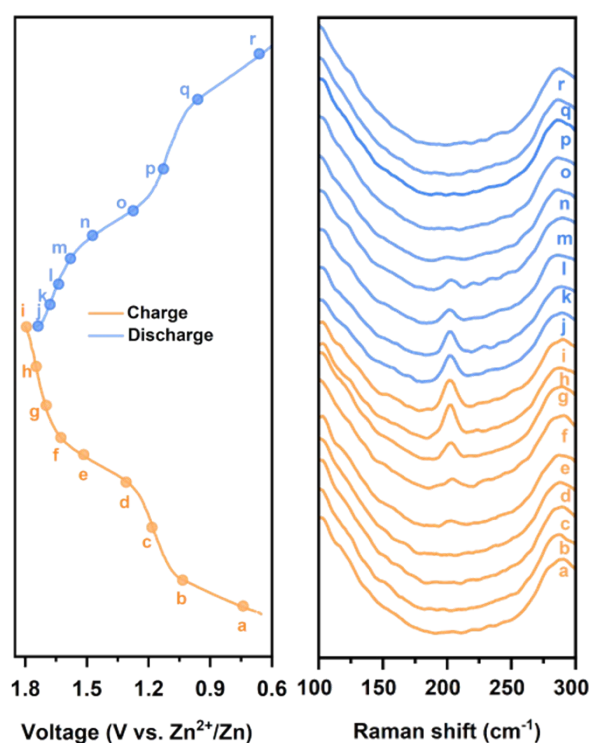**Fig. S21.** In-situ Raman spectra and the corresponding time–voltage curve with the HE 2-16 electrolyte.

During charge from 1.4 V to 1.8 V, Raman signal emerged around 202 cm^{-1}, corresponding to the formation of ICl species in **Fig. S21** (*Nat Commun.*, 2021, 12, 170; *Energy Environ. Sci.,* 2021, 14, 407–413). Therefore, iodine species undergo a reversible and complete transformation including I$^-$ $\rightleftharpoons$ I$_2$ $\rightleftharpoons$ ICl. Based on the electrochemical analysis and spectral results, we depict a clear portrait of the reaction mechanism for the four-electron iodine conversion.

The four-electron conversion mechanism are summarized as below:

Cathode:

2 I$^-$ $\leftrightarrow$ I$_2$ + 2 e$^-$ $\qquad$ E = 0.53 V vs. SHE

I$_2$ + 2 Cl$^-$ $\leftrightarrow$ 2 ICl + 2 e$^-$ $\qquad$ E = 1.07 V vs. SHE

Anode: Zn^{2+} + 2 e$^-$ $\leftrightarrow$ Zn $\qquad$ E = −0.76 V vs. SHE

Total reaction:

Zn^{2+} + 2 I$^-$ $\leftrightarrow$ Zn + I$_2$ + 2 e$^-$ $\qquad$ E= 1.29 V

Zn^{2+} + I$_2$ + 2 Cl$^-$ $\leftrightarrow$ Zn + 2 ICl + 2 e$^-$ $\quad$ E= 1.83 V
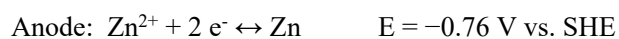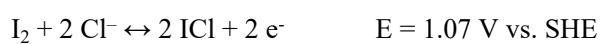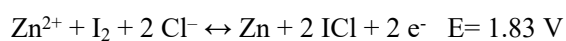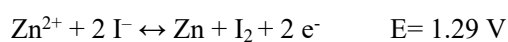
Fig. S22. GCD profiles of batteries with HE 2-18 at different current densities.

Supplementary Notes:

The detailed information about the hybrid electrolyte for suppressing the side reactions.

Supplementary Note 1
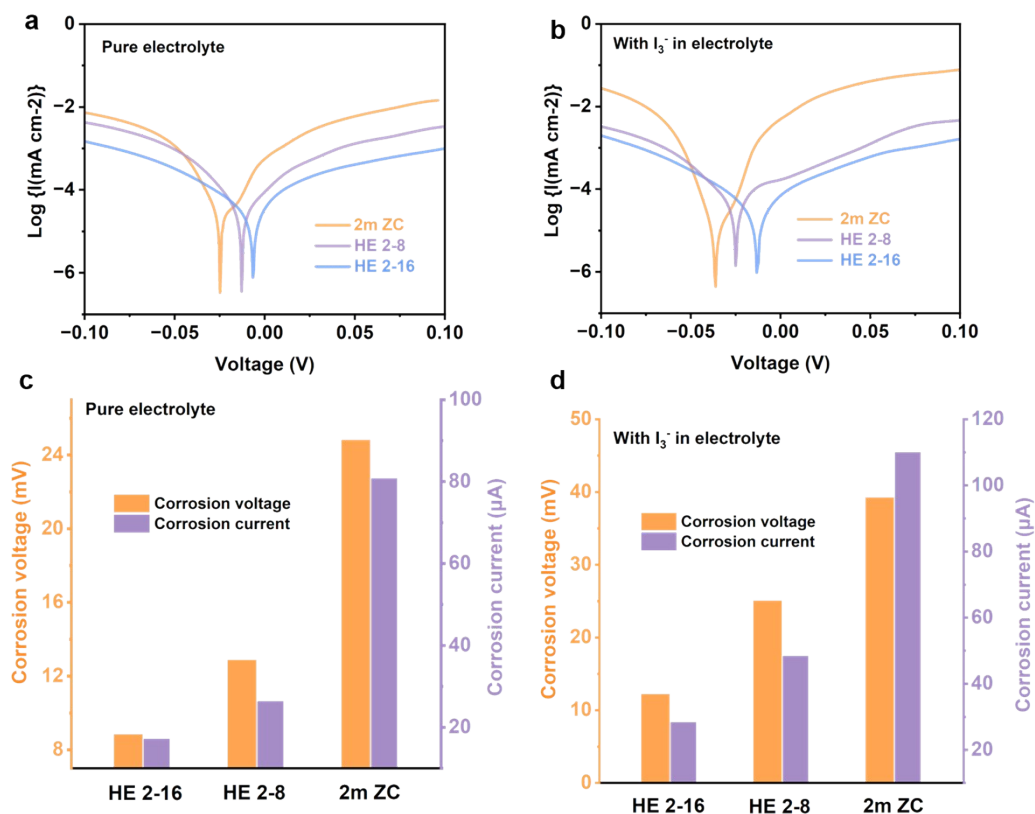
Fig. N1. Linear polarization curves showing the corrosion of various electrolyte (a) without I_3^- ions or (b) with I_3^- ions at 1 mV s^{-1}. The corrosion voltage and corrosion current of zinc anode various electrolyte (c) without I_3^- ions or (d) with I_3^- ions.

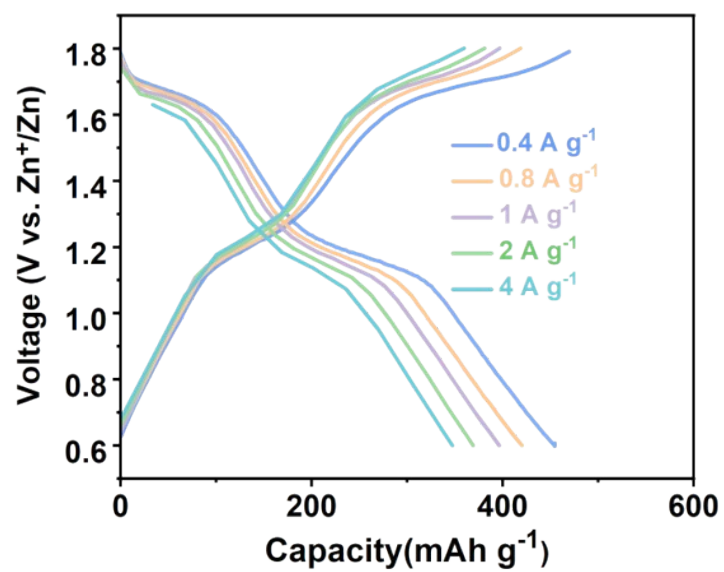The corrosion-resistant performances were test through electrochemical tests. The suppressed Zn corrosion was initially evidenced by Tafel polarization curves in Zn‖Zn symmetric cells with different electrolytes (**Fig. N1a-N1b**), in which the corrosion voltage and the corrosion current density in the ZC electrolyte (24.8 mV and 80.7 μA cm^{-2}) corresponds to 281.8% and 530.4% of the value obtained for the HE 2-16 electrolyte (8.8 mV and 17.1 μA cm^{-2}) (**Fig. N1c**). The decrease in corrosion voltage and corrosion current density suggests its diminished corrosion rate as shown in **Fig. N1c**. However, the corrosion rate in all electrolytes will be accelerated when adding I_3^- ions in the electrolyte (**Fig. N1d**). It is worth noting that the corrosion rate is still very slow in HE 2-16 electrolyte compared other electrolytes when intermediates I_3^- ions existing.

Supplementary Note 2
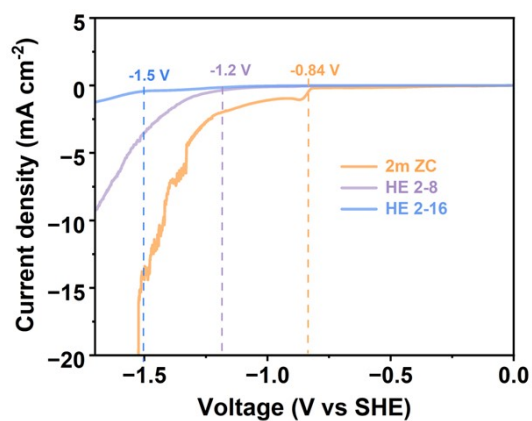
Fig. N2. LSV curves recorded under of various electrolytes (Sodium chloride replace Zinc chloride to prepare electrolytes for excluding the effects of competing Zn deposition process).

The hydrogen evolution reactions (HER) activity was assessed using linear sweep voltammetry (LSV) measurements, and the lower onset HER potential for HE 2-16 manifests a reduced susceptibility to corrosion, potentially attributed to the reduced water activity (**Fig. N2**).

Supplementary Note 3
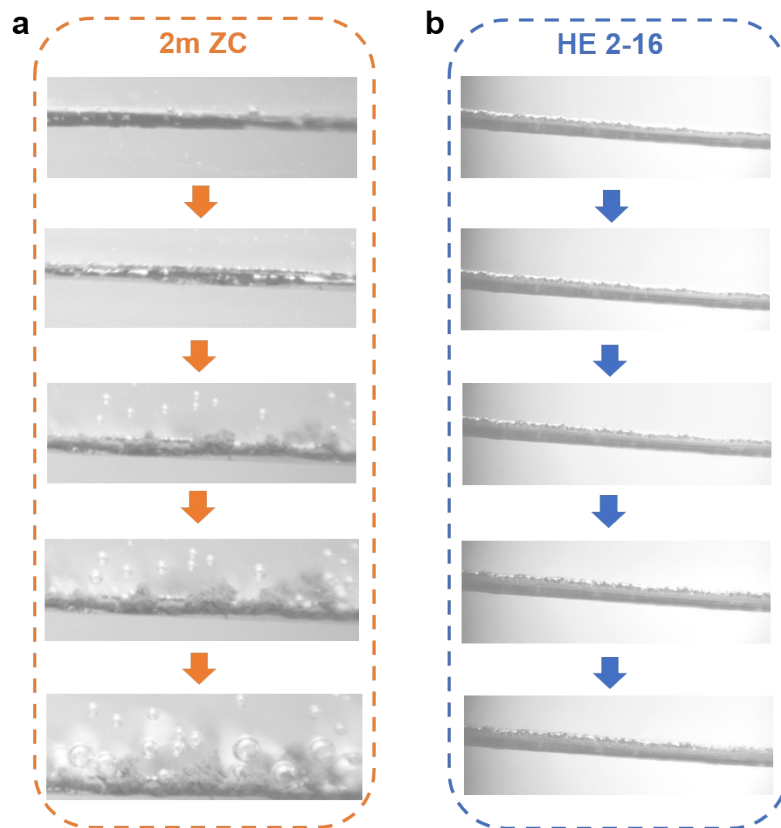
Fig. N3. *In-situ* optical microscopy investigations of the Zn deposition using (a) Pure ZnCl$_2$ electrolytes and (b) HE 2-16.

To access the impact of I$_3^-$ ions on the zinc plating/stripping process, we conducted investigations using Zn-iodine cells from *in-situ* optical microscopy (**Fig. N3**). For pure ZnCl$_2$ electrolyte, large amount of dendrite and copious bubbles were observed in the anode–electrolyte interface, as depicted in **Fig. N3a**. While for hybrid electrolyte, only a relatively smooth deposition layer was generated after fully charged with a current density of 2 mA cm^{-2} (**Fig. N3b**).

Supplementary Note 4
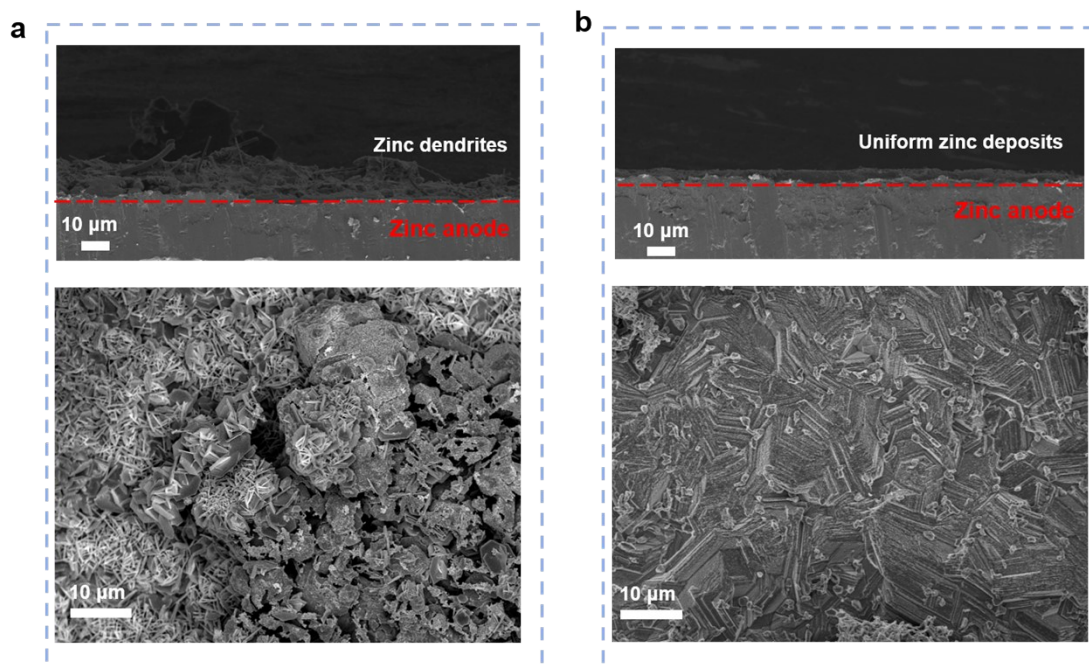
Fig. N4. Cross-section and plane SEM images of the zinc anodes (a) HE 2-16 electrolyte and (b) 2m ZC electrolyte after 50 cycles.

Due to the strong interaction between Zn^{2+} and OTf^-, the high C_{OTf^-} can guide the rapid transfer of Zn^{2+} to the surface of the Zn anode, thereby accelerating the reaction kinetics and promoting uniform Zn deposition (**Fig. N4**). Upon zinc stripping at the 50th cycles, a thick layer of "dead zinc" with a loosened, stacked structure can be found (**Fig. N4a**). In sharp contrast, a compact and uniform surface can be observed using the high C_{OTf^-} electrolyte, which effectively impeded the dendrite growth (**Fig. N4b**). This is also consistent with the electrochemical results.

Supplementary Note 5

Fig. N5. The cycling performance of 4eZIBs of coin cells with (a) the pure 2m ZC and (b) HE 2-16 electrolytes. The optical image of a coin cells before and after cycling.

Supplementary Note 6

Fig. N6. Galvanostatic charge and discharge (GCD) profiles of various electrolytes at 0.4 A g^{-1}.

Supplementary Note 7

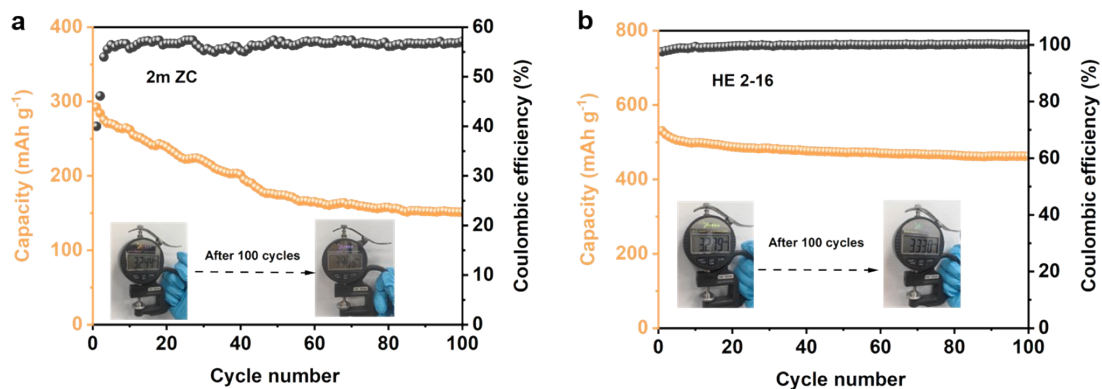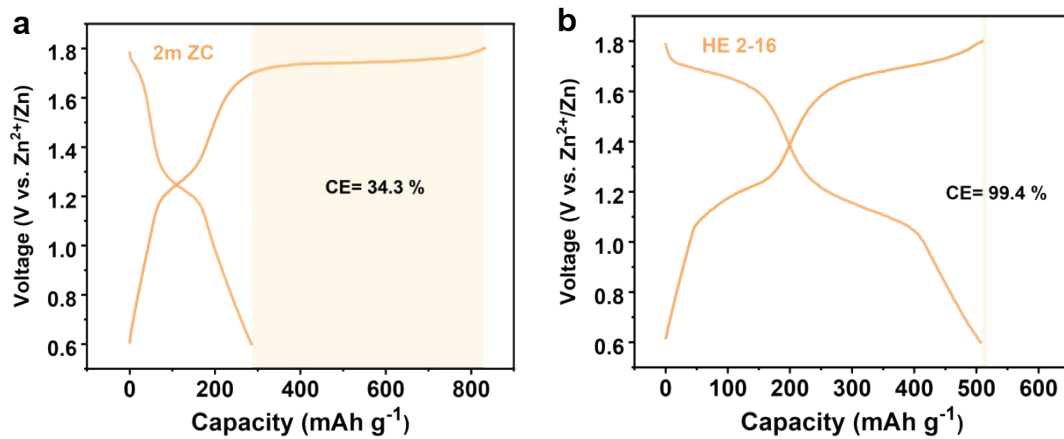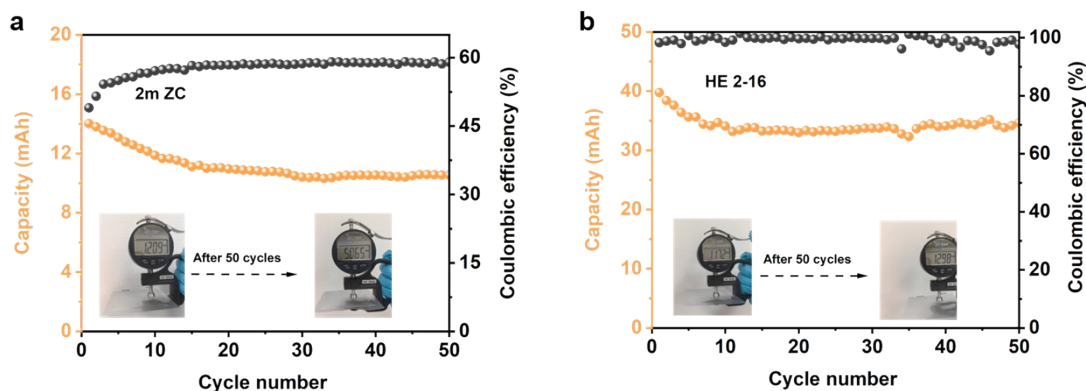**Fig. N7**. The cycling performance of 4eZIBs of soft package batteries with (a) the pure 2m ZC and (b) HE 2-16 electrolytes. The optical image of soft package batteries before and after cycling.

We assembled a series of soft package batteries and coin cells with 2m ZC and HE 2-16 electrolytes to confirm the practical application of 4eZIBs. Evidently, 4eZIBs employing the HE 2-16 exhibits a high specific capacity of 462.2 mAh g^{-1} after 100 cycles, with a superior capacity retention ratio of 97.2%, compared to the 2m ZC electrolyte with poor coulombic efficiency (151.2 mAh g^{-1}, 51.7%) (**Fig. N5**). The distinct battery swelling is observed in **Fig. N5** after cycling because of the hydrogen evolution reactions (HER) and Cl_2 gas evolution, which could be proved by **Fig. N3** and **N6** (*Nat Commun*, 2023, 14, 4211; *Nat Commun*, 2023, 14, 1856; *Nat Commun*, 2023, 14, 7080). The overcharging chlorine-containing electrolyte under high voltage will lead to the precipitation of chlorine with iodine electrodes as shown in **Fig. N6** (*Nat Commun*, 2023, 14, 1856; *Angew. Chem. Int. Ed.* 2023, 62, e202310168), however, gaseous chlorine is irreversible in this system. The HER and Cl_2 gas evolution inevitably occurs on the anode and cathode sides, which decreases the Coulombic efficiency (CE) and cycling stability of the batteries. While, this phenomenon also occurs in soft package batteries, which could be seen in **Fig. N7**. The assembled pouch cell using HE 2-16 showed improved cycling stability and a reversible areal capacity of 3.1 mAh cm^{-2} after 50 cycles at 5 mA cm^{-2} with a coulombic efficiency of 99.8%. On the contrary, the soft battery with 2m ZC electrolyte has low capacity and coulombic efficiency, which lead to soft battery swelling (**Fig. N7**).

Table S1. The numbers of molecules in the hybrid electrolytes used for MD simulations.

Number of	Zn^{2+}	Cl^-	H_2O	Li	OTf^-
2 m ZC	40	80	1100	0	0
HE 2-8	40	80	4800	160	160
HE 2-16	40	80	1800	320	320

Table S2. Comparison of various Zn-I$_2$ aqueous batteries

	Cathode hosts, output voltage	Electrolyte	Specific capacity (mAh g^{-1})	Capacity retention	Ref
2eZIBs (I$^-$/I$_2$)	ACF-I$_2$; 1.22 V	1M ZnSO$_4$	174.4 (0.2 A g^{-1})	90 %,3000	[1]
	ACC/I$_2$; 1.21 V	1M ZnSO$_4$	211 (0.2 A g^{-1})	90%,1500	[2]
	Co[Co$_{1/4}$Fe$_{3/4}$(CN)$_6$]/I$_2$; 1.26 V	2M ZnSO$_4$	236.8 (0.2 A g^{-1})	83.6%,1500	[3]
	B−Fe−NC/I$_2$; 1.27 V	2M ZnSO$_4$	220 (0.2 A g^{-1})	71%,10000	[4]
	PNC-1000-I$_2$; 1.26 V	1M ZnSO$_4$	252 (0.2 A g^{-1})	75%,10000	[5]
4eZIBs (I$^-$/I$_2$/I$^+$)	PAC/I$_2$; 1.19 V/1.61 V	19 m ZnCl$_2$ + 19 m LiCl	589 (0.4 A g^{-1})	90.8%,6000	[6]
	I$_2$@C; 1.18 V/1.59 V	hydrated eutectic electrolyte Zn(ClO$_4$)$_2$·6H$_2$O: DMS: NA	412 (0.5 A g^{-1})	80%,2000	[7]
	AC/I$_2$; 1.26 V/1.63V	2m ZnCl$_2$ + 16 LiOTf	483 (0.4 A g^{-1}); 377 (2 A g^{-1})	83.6%,10000	**This work**

References

[1] Pan, H.; Li, B.; Mei, D.; Nie, Z.; Shao, Y.; Li, G.; Li, X.; Han, K.; Mueller, K.; Sprenkle, V.; Liu, J., Controlling solid–liquid conversion reactions for a highly reversible aqueous zinc–iodine battery. *ACS Energy Letters*, **2017**, 2(12), 2674-2680. https://doi.org/ 10.1021/acsenergylett.7b00851.

[2] Bai, C., Cai, F., Wang, L., Guo, S., Liu, X., Yuan, Z. A sustainable aqueous Zn-I$_2$ battery. *Nano Research*, 2018, 11, 3548-3554. https://doi.org/10.1007/s12274-017-1920-9.

[3] Ma, L.; Ying, Y.; Chen, S.; Huang, Z.; Li, X.; Huang, H.; Zhi, C. Electrocatalytic Iodine Reduction Reaction Enabled by Aqueous Zinc-Iodine Battery with Improved Power and Energy Densities. *Angew. Chem., Int. Ed.* **2021**, 133 (7), 3835–3842. https://doi.org/10.1002/ange.202014447.

[4] Liu, M.; Chen, Q.; Cao, X.; Tan, D.; Ma, J.; Zhang, J. Physicochemical Confinement Effect Enables High-Performing Zinc–Iodine Batteries. *J. Am. Chem. Soc.* **2022**, 144 (47), 21683–21691. https://doi.org/10.1021/jacs.2c09445.

[5] Liu, T.; Wang, H.; Lei, C.; Mao, Y.; Wang, H.; He, X.; Liang, X. Recognition of the Catalytic Activities of Graphitic N for Zinc-Iodine Batteries. *Energy Storage Mater.* **2022**, 53, 544–551. https://doi.org/10.1016/j.ensm.2022.09.028.

[6] Zou, Y.; Liu, T.; Du, Q.; Li, Y.; Yi, H.; Zhou, X.; Li, Z.; Gao, L.; Zhang, L.; Liang, X. A Four-Electron Zn-I2 Aqueous Battery Enabled by Reversible $I^-/I_2/I^+$ Conversion. *Nat. Commun.* **2021**, 12 (1), 170. https://doi.org/10.1038/s41467-020-20331-9.

[7] Li, W.; Xu, H.; Zhang, H.; Wei, F.; Zhang, T.; Wu, Y.; Huang, L.; Fu, J.; Jing, C.; Cheng, J.; Liu, S. Designing Ternary Hydrated Eutectic Electrolyte Capable of Four-Electron Conversion for Advanced Zn–I_2 Full Batteries. *Energy Environ. Sci.* **2023,**16, 4502-4510**.** https://doi.org/10.1039/D3EE01567J.